Materials Science & Engineering A 831 (2022) 142319

Contents lists available at ScienceDirect

Materials Science & Engineering A

journal homepage: www.elsevier.com/locate/msea

Role of martensitic transformation sequences on deformation-induced martensitic transformation at high strain rates: A quasi in-situ study

Minghao Huang [a], Jiahua Yuan [a], Jinliang Wang [b], Lingyu Wang [a], A. Mogucheva [c], Wei Xu [a,*]

[a] State Key Laboratory of Rolling and Automation, School of Materials Science and Engineering, Northeastern University, Shenyang, 110819, China
[b] School of Mechanical and Power Engineering, Guangdong Ocean University, Zhanjiang, 524000, China
[c] Laboratory of Mechanical Properties of Nanoscale Materials and Superalloys, Belgorod State University, Belgorod, 308015, Russia

ARTICLE INFO

Keywords:
Strain rate
Deformation-induced martensitic transformation
Nucleation
Martensitic transformation sequence
Variant selection

ABSTRACT

For the mechanical behavior of steels with metastable austenite, it was widely accepted that high strain rates could weaken deformation-induced martensitic transformation (DIMT) and reduce work-hardening behavior. This limits the application of these steels for energy-absorption applications, e.g., impact conditions. However, the mechanism of strain-rate dependent DIMT is still not well understood and it greatly limited the further alloy design. Thus, with the aim of revealing the intrinsic relations between strain rate and martensitic transformation, quasi-in-situ EBSD (Electron Backscatter Diffraction) tests were performed under different strain rates in this study. The influence of the martensitic transformation sequences on the DIMT volume fraction was investigated. With increasing strain rate, the γ→ε→α' transformation was inhibited, and the γ→α' transformation sequences dominated. The martensitic transformation sequences firstly affect the nucleation behavior. The α′-martensite nucleation sites changed from ε or twin to twin only, and thus, the α′-martensite nucleation barrier increased. In addition to nucleation, the variant selection phenomenon caused by the absence of ε-martensite under high strain rates increased the elastic strain energy, which inhibited the growth of α′-martensite. By affecting both nucleation and growth, high strain rates suppress the γ→ε→α' transformation, and inhibit DIMT kinetics. Thus, by tailoring the martensitic transformation sequences, two methods are proposed to enhance DIMT behavior via suitable control of the stacking fault energy. This work provides a comprehensive explanation for the strain-rate dependence of DIMT, which can be used to tailor the mechanical properties of steels with metastable austenite.

1. Introduction

Transformation-induced-plasticity (TRIP)-assisted steels are mainly characterized by metastable austenite microstructure, and have both high strength and plasticity [1]. These steels have garnered significant attention owing to the deformation-induced martensitic transformation (DIMT) process that increases their work-hardening ability and delays necking during deformation processes [1,2]. Particularly for TRIP-assisted steels used in the automotive industries, dynamic testing is of significant practical importance [3]. Studies have reported that DIMT behavior is suppressed under high strain rates [4–6], where limited TRIP effects correspond to a weakened work-hardening index and unfavorable mechanical properties [7,8]. Hence, to facilitate the informed design of TRIP-assisted steel, further study is required on DIMT behavior under dynamic loads, which would then assist the development of tailored metastable austenite.

Martensitic transformation behavior under different strain rates has been extensively studied, both experimentally and through modeling. Because the growth of α′-martensite occurs through repeated nucleation, many studies have focused on the martensite nucleation sites [9,10]. It has been shown that the number of effective nucleation sites for α′-martensite decrease with increasing strain rate, thus reducing the volume fraction of α′-martensite. Although various studies have reached the same conclusion, they propose quite different causes. It has been claimed that an increase in temperature caused by the high strain rate negatively affects the shear band intersections [11,12], which are the primary nucleation sites for α′-martensite [13,14]. Similarly, a modeling study showed that increasing temperature decreases the rate of shear band formation, and suppresses driving shear band crossing [15]. Other studies [16,17] claimed that stacking faults (SFs) must overlap significantly before α′-martensite nucleation occurs, and thus, increasing the temperature may hinder the formation of shear bands of sufficient

* Corresponding author.
E-mail address: xuwei@ral.neu.edu.cn (W. Xu).

https://doi.org/10.1016/j.msea.2021.142319
Received 15 August 2021; Received in revised form 5 November 2021; Accepted 8 November 2021
Available online 11 November 2021

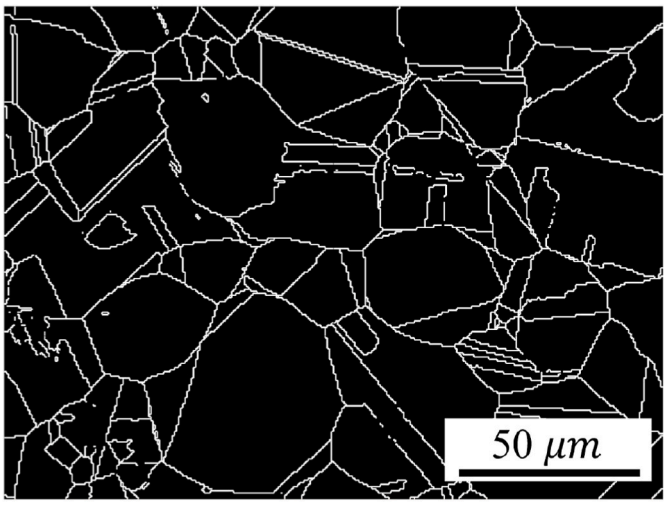

Fig. 1. Austenite phase map of the tempered 321 stainless steel (white lines represent grain boundaries).

thickness [9]. Furthermore, the relationships between SF characteristics and the nucleation sites of α′-martensite, which influence the DIMT behavior kinetics, have been studied [17,18]. In addition to the nucleation sites, the chemical driving forces ($\Delta G_{\gamma\rightarrow\alpha'}$) [9,19,20] caused by adiabatic heating [1,21–24] during the loading process have been reviewed by H Mirzadeh et al. These driving forces also play a key role in explaining the suppressed DIMT behavior under dynamic loading. As this previous studies [21–24] elaborated, the DIMT behavior under various strain rates is consistently related to adiabatic heating.

In contrast, Vázquez-Fernández et al. [10] argue that suppressed DIMT under dynamic loading is almost temperature independent. In that study, α′-martensite variant selection was observed under dynamic loading conditions. It was proposed that α′-martensite primarily nucleates on a single habit plane (limited α′-martensite nucleation sites), finally resulting in an inhibited DIMT process. The conflicting conclusions in the literature make it difficult to accurately tailor the austenite microstructure, mainly due to a lack of characterization data obtained during the martensitic transformation process. Thus, further study of martensitic transformation behavior under various strain rates and temperatures is required.

In this paper, further study of the mechanisms behind the observed relationship between DIMT and strain rate, and its effect on TRIP-assisted steel design, is considered. Based on previous researches, this study express the effect of strain rate on the martensitic transformation sequences and the resulting volume fraction of martensite. Through quasi-in-situ tracking of martensitic transformation behavior under dynamic and quasi-static loading, the change in martensite volume fraction was examined. Additionally, the study proposes a strategy for optimizing the dynamic mechanical properties through controlling the stacking fault energy (SFE).

2. Materials and methods

In this study, a commercial 321 stainless steel sheet with 15 mm in thickness was selected as the experimental material due to its mechanically metastable characteristic. The commercial steel sheets were cold rolled to 12 mm thickness and then tempered at 1173K for 0.5h. This resulted in a homogeneous microstructure, as shown in Fig. 1. In which black represent for austenite phase and the white line represents grain boundaries. The chemical compositions of the present sheets are listed in Table 1.

For the dynamic (Charpy loading) and quasi-static three-point bending tests, the stainless steel was machined into standard V-notch Charpy impact specimens (dimensions: 10 × 10 × 55 mm^3). The three-point-bending rig comprised supports and indenters, as shown in Fig. 2, with the two lower supports 40 mm apart, while the upper indenter was the same size as the impact pendulum (blade radius 2 mm). To observe the microstructural evolution, interrupted Charpy testing was conducted. For the loading tests, the Charpy impact tests used an MTS impact tester (SANS ZBC2452-C) with 1 J resolution; the quasi-static three-point-bending tests used a universal testing machine (Shimadzu AG-X) at a constant strain rate of 2 mm/min.

For ease of microstructural characterization, before the loading tests were conducted, the samples were meticulously electropolished at −20 °C with a voltage of 20 V for 20 s. Microstructural characterization focused on the root of the V-notch area, using quasi-in-situ microbeam

Table 1
Chemical composition (wt.%).

C	Si	Mn	Cr	P	S	Ni	N	Ti	Fe
0.021	0.578	1.384	17.56	0.033	0.0004	9.337	0.004	0.252	Balance

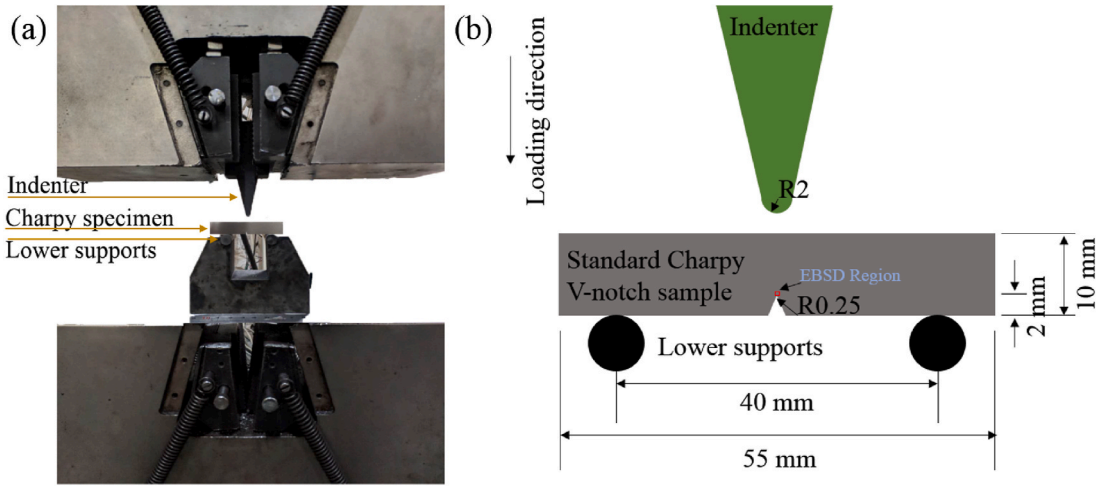

Fig. 2. (a) Quasi-static three-point-bending test setup. (b) Schematic diagram of quasi-static three-point-bending test and characterization region.

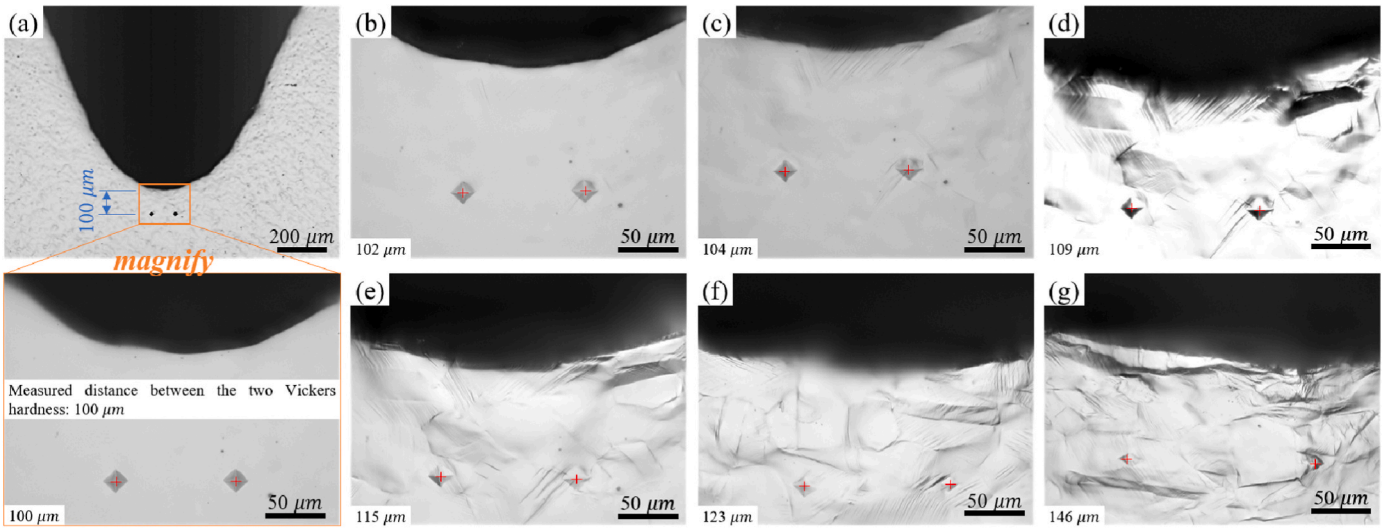

Fig. 3. The determine of nominal strain near the root of V-nothc (a) 0% nominal strain; (b) 2% nominal strain; (c) 4% nominal strain; (d) 9% nominal strain; (e) 15% nominal strain; (f) 23% nominal strain; (b) 46% nominal strain.

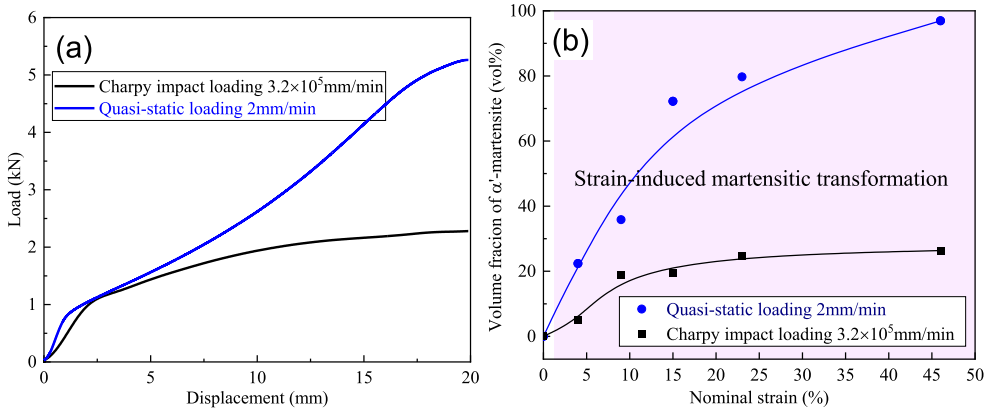

Fig. 4. (a) Load-displacement curves of SUS321 stainless steel at varying strain rates. (b) Martensite fraction as a function of nominal strain.

X-ray diffraction (XRD; D8 Discover) and quasi-in-situ electron backscatter diffraction (EBSD; Zeiss Ultra55 equipment with an EBSD detector of Oxford Instruments Aztec). The phases volume fraction based on micro-beam XRD results was calculated based on the review of H Mirzadeh et al. [20]. The EBSD data was interpreted using AZtecCrystal analysis software.

Charpy V-notch causes strain and stress concentration on the root of V-notch, which makes it hard to measure the strain during the test. To determine the extent of deformation in the quasi-in-situ test, the quantification of nominal strain was carried out. In detail, two Vickers indents with 100 μm distance were located at the root of V-notch before loading tests, as shown in Fig. 3(a). And then tested under the MTS impact tester with a given energy, as shown in Fig. 3(b–g). Which were used to accurately monitor the changes in the plastic strain, as in our previous study [25]. Thus the nominal strain was obtained through the displacement increment between two Vickers indents divide by the initial distance between two Vickers indents (100 μm).

3. Results

3.1. Martensitic transformation behavior under quasi-static and dynamic loading

Fig. 4(a) shows the load-displacement curves obtained at different strain rates, prior to crack initiation. As compared in Fig. 4(a), the value of load increases with the increasing displacement of the hammer for both quasi-static and dynamic loading conditions. However, the load increases sharply with the increasing displacement at quasi-loading conditions, while the load slightly increased with the increasing displacement at Charpy impact tests. The load-displacement curves directly reflect that the increasing strain rates resulted in a weakened work-hardening rate. The work-hardening behaviour shows a strong negative strain rates sensitivity, as indicated in previous studies [8]. As H Mirzadeh et al. [1] and P.Barriobero-Vila et al. [26] directly built the positive relations between work-hardening rate and strain-induced α′-martensite volume fraction. The volume fraction of α′-martensite takes a significant role in dynamic mechanical properties. Thus, the α′-martensite volume fraction during Charpy impact and quasi-static loading has been studied, as shown in Fig. 4(b). For similar strain conditions, the quasi-static testing results showed a higher volume fraction of α′-martensite, resulting from an enhanced TRIP effect and work-hardening behavior. The volume fraction of α′-martensite under Charpy impact loading increased with increasing strain, and reached saturation (~20 vol%) at approximately 10% nominal strain. However, for steel deformed through quasi-static loading, the volume fraction of α′-martensite increased with the increasing strain until the metastable austenite almost fully transformed to α′-martensite.

The tendency of α′-martensite volume fraction to change with

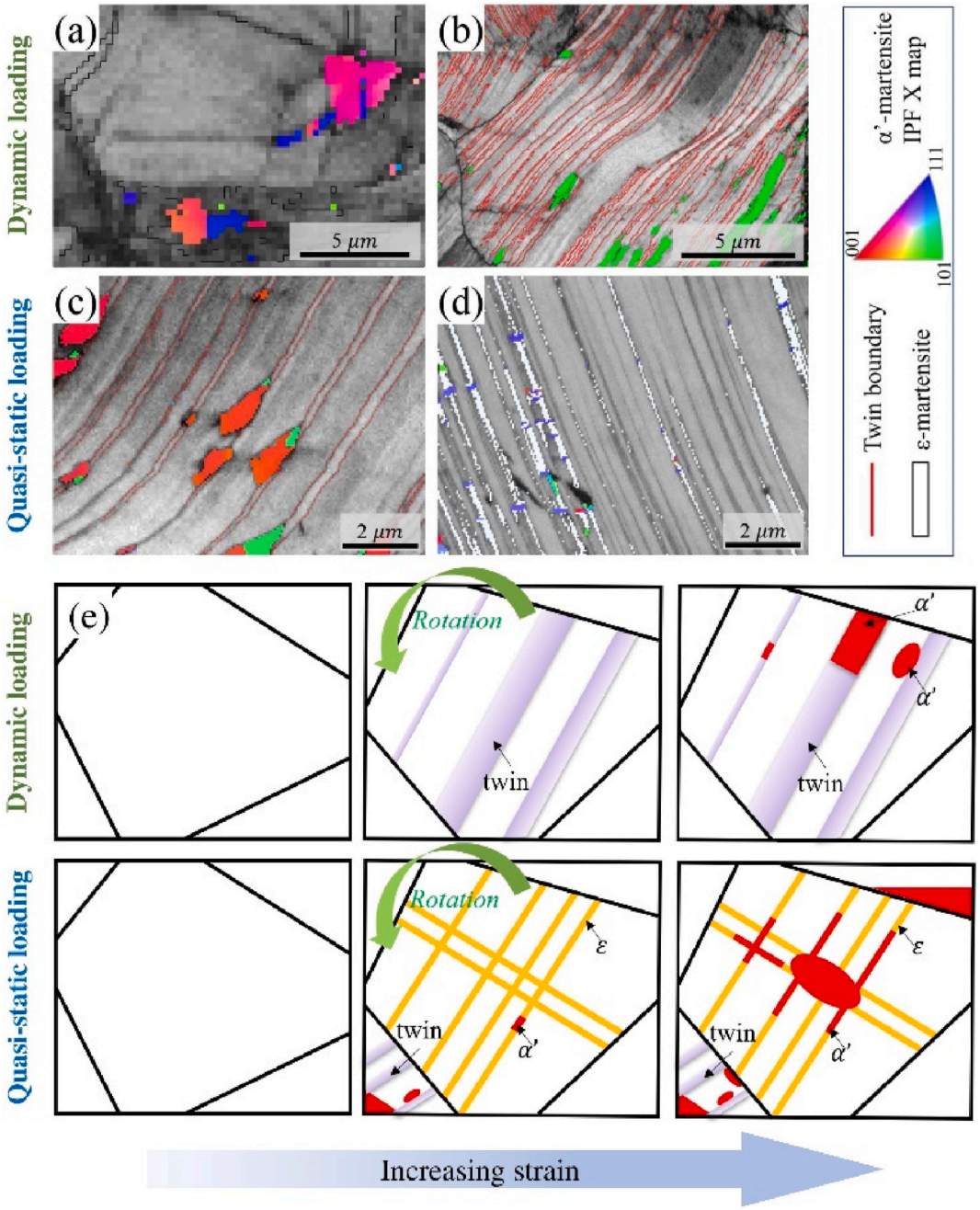

Fig. 5. EBSD maps and loading schematic. EBSD of (a) colored BCC IPF X and (b) BC map of dynamic loading at 4% nominal strain; (c) Colored BCC IPF X, white ε-martensite phase, and (d) BC map of static loading at 4% nominal strain. (e) Schematic illustrations of the dynamic and static loading martensitic transformation for γ→ε→α′ and γ→α′ sequences.

loading rates agrees with findings from previous studies. However, notably, the difference in α′-martensite volume fraction (~80%) observed between dynamic and quasi-static loading is larger than previously reported (~50% different in J. Talonen et al.' study [5] or ~30% different in N.I. Vázquez-Fernández et al.'study [9]). Thus, the explanations proposed by previous studies may not be valid in the present case. In summary, the limited DIMT behavior under dynamic loading is responsible for the lower work-hardening rate [20,26], although the considerable difference in α′-martensite volume fraction between dynamic and quasi-static loading needs further study.

3.2. *Effect of strain rate on the nucleation sites of α'-martensite*

To further study the observed reduction in the α′-martensite volume fraction with increasing strain rates, the nucleation of α′-martensite during plastic deformation was investigated in detail using the EBSD method, as shown in Fig. 5. In these maps, ε-martensite and α′-martensite are shown in white and IPF X (inverse pole Fig. X) colors, respectively, and the red lines indicate the twin boundaries. As seen in our previous studies, DIMT facilitates nucleation at the deformation bands and grain boundaries [25]. Thus, for α′-martensite nucleation, both the number and type of the deformation bands need to be considered. Talonen et al. [9] examined the influence of strain rate on the number of deformation bands, and suggested that an increasing strain rate decreases the number of effective α′-martensite nucleation sites. However, Fig. 5(a) and (b) show that, under dynamic loading conditions, the α′-martensite nucleates at the grain boundaries and twinning boundaries. Additionally, under the quasi-static loading conditions, the

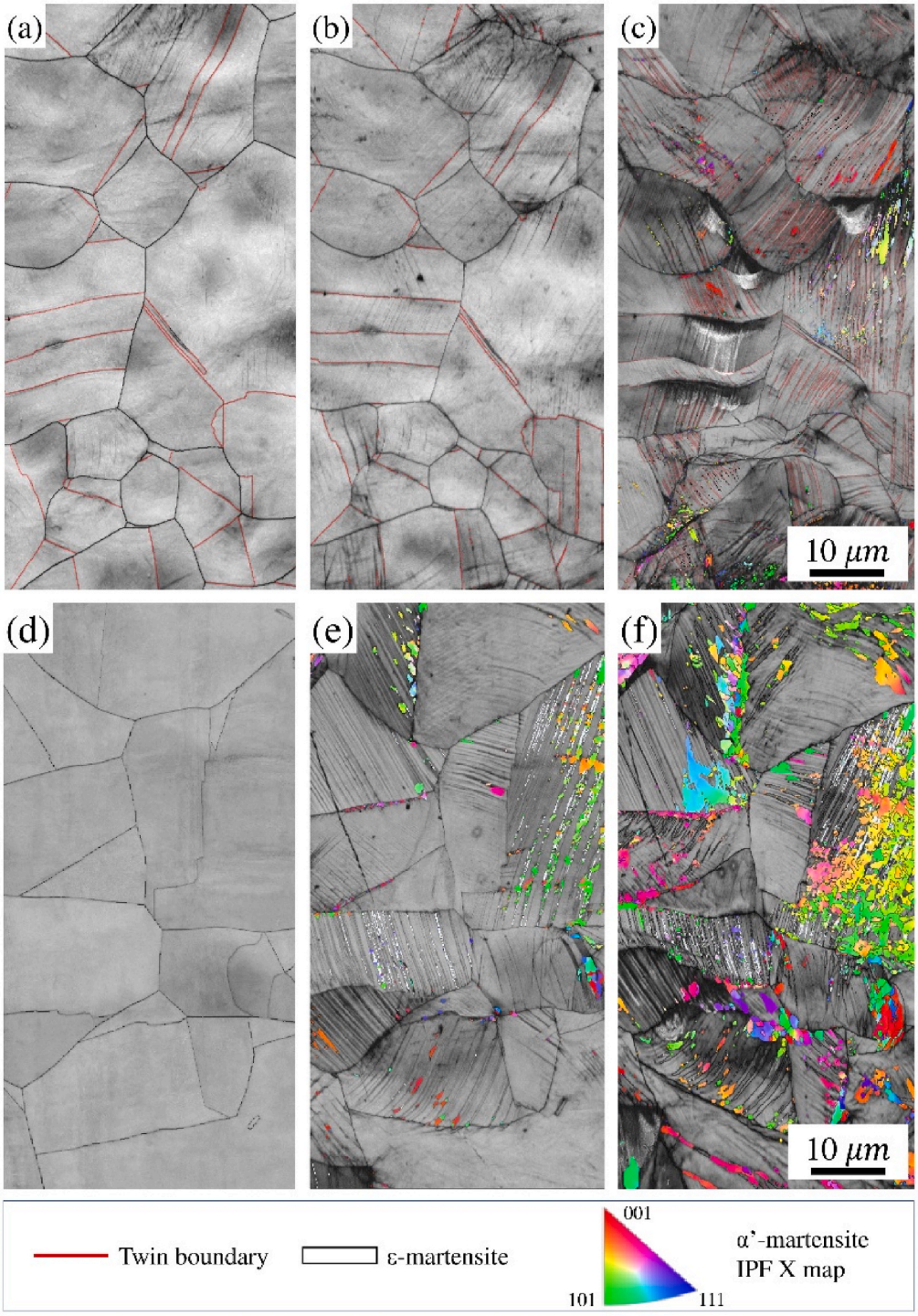

Fig. 6. Colored BCC IPF X, white ε-martensite phase, and BC map of specific areas subjected to dynamic loading conditions with (a) 0%, (b) 2%, and (c) 4% nominal strain, respectively; and static loading with (d) 0%, (e) 2% and (f) 4% nominal strain, respectively.

nucleation sites partially changed from the twinning boundaries to ε-martensite (Fig. 5(c) and (d)). Under quasi-static loading conditions, some of the deformation bands had an hcp structure, which is the most favorable for α′-martensite nucleation [20,27]. Because of the ε-martensite created during quasi-static loading, the nucleation barrier of α′-martensite changes from $\Delta G_{\gamma\rightarrow\alpha'}$ to $\Delta G_{\varepsilon\rightarrow\alpha'}$. To quantify the nucleation barrier of α′-martensite, the difference in Gibbs free energy between bcc, fcc, and hcp phases (i.e., $\Delta G_{\gamma\rightarrow\alpha'}$ to $\Delta G_{\varepsilon\rightarrow\alpha'}$) at 298 K was thermodynamically calculated by a commercial thermodynamics calculation program, ThermoCalc2017 with the TCFE9 database. The corresponding Gibbs free energy was found to decrease from 2795 to 2202 J/mol. A schematic of the α′-martensitic transformation process under different strain rates is shown in Fig. 5(e).

Under dynamic-loading conditions, the restricted ε-martensite formation is responsible for the suppressed martensitic transformation behavior. Additionally, the martensitic transformation sequences are believed to play a significant role in DIMT behavior [28]. Since the SFE value is usually used to predict and evaluate the deformation behavior of fcc metals, this study uses a thermodynamics model [29] to calculate the SFE, as previous studies. As a result, SFE is linearly dependent on

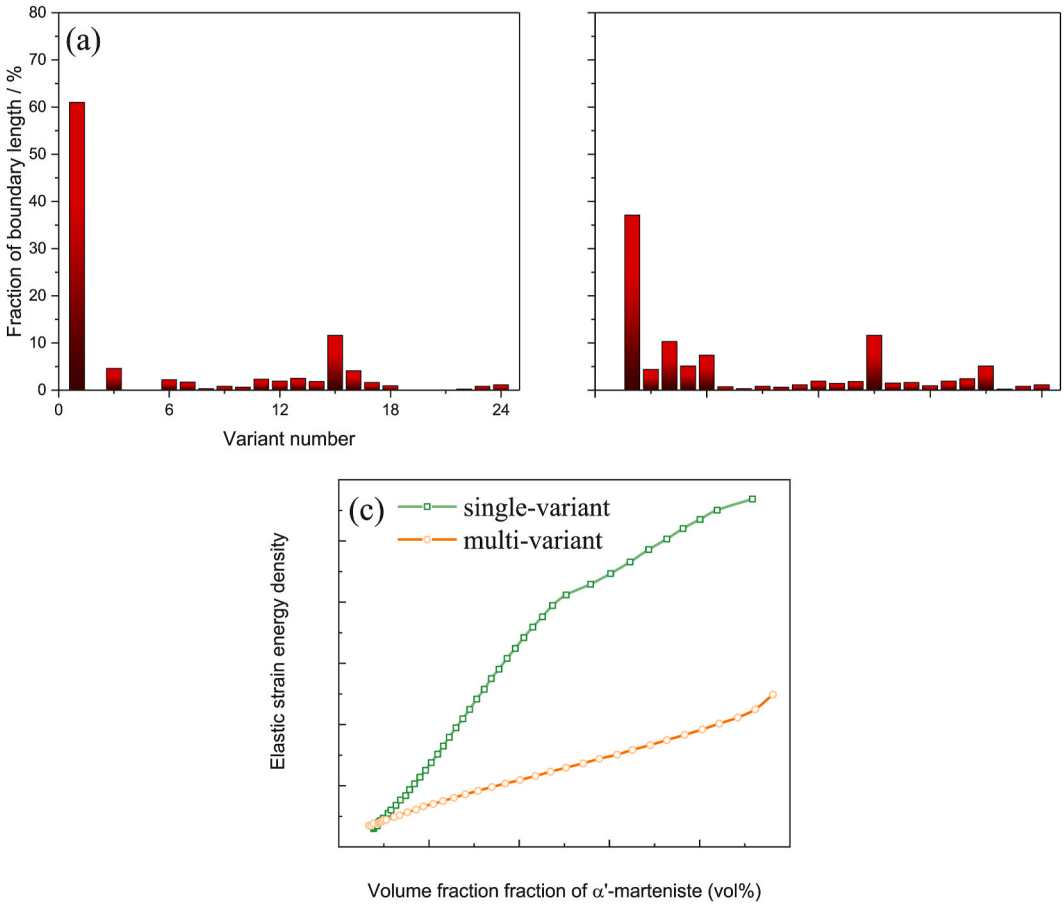

Fig. 7. (a) and (b) Variant pairing distributions in α'-martensite for specimens deformed to a nominal strain of 4% under dynamic and quasi-static loading, respectively; (c) the calculated elastic strain energy density of α'-martensite.

temperature, with a temperature coefficient of 0.103 mJ m^{-2} C^{-1}. Under quasi-static loading conditions, and assuming a temperature of 25 °C, the calculated SFE is approximately 25 mJ m^{-2}. However, in the case of higher strain rates, the temperature increase (~150 °C)caused by the adiabatic heating during the Charpy test [30], increased the SFE to 37.9 mJ m^{-2}. Varying the strain rates resulted in significant changes in the SFE, and accordingly, variations in the martensitic transformation sequences. Hence, the dominant deformation mechanism depends on the SFE value. Overall, when estimating the DIMT volume fraction, the SFE value should be considered, and it is especially significant at high strain rates.

3.3. *Influence of variant selection on the growth of α′-martensite under high strain rates*

Martensitic transformation behavior depends on the nucleation and growth of α′-martensite, which are both affected by varying the strain rate. From a thermodynamics point of view, previous studies [19] on the relationships between strain rate and the growth of α′-martensite primarily focused on the chemical driving force caused by adiabatic heating. Similarly, based on the classical martensitic transformation theory, the elastic strain energy produced during the shear process of martensite formation is also drawing research attention.

During martensitic transformation, variant selection is believed to play a significant role in determining the strain energy and transformation kinetics. Vázquez-Fernández et al. [10] showed that high strain rates produce changed martensite variant selection, and similar phenomena are observed in this study, as shown in Fig. 6. The martensite variants are numbered based on Morito et al.'s study [31] and our previous study [25], and the statistical results are shown in Fig. 7(a) and (b).

The strain energy densities for single-variant and multi-variant α'-martensite were calculated based on [32]:

$$G_v^{el} = \int_{\epsilon_{ij}^0(r)}^{\epsilon_{ij}(r)} \sigma_{ij}(r) d\epsilon_{ij}(r) = \int_{\epsilon_{ij}^0(r)}^{\epsilon_{ij}(r)} c_{ijkl}(\epsilon_{kl}(r) - \epsilon_{kl}^0(r) - \epsilon_{kl}^{pl}(r)) d\epsilon_{ij}(r) \quad (1)$$

where V is the total volume of the system, $\varepsilon^o(r)$ are stress-free transformation strains, ε(r) are actual strains,σ_{ij} is the elastic stress,c_{ijkl} is the tensor of the elastic moduli, and $\varepsilon_{kl}^{pl}(r)$ is the plastic strain. The results are shown in Fig. 7(c). At a given volume fraction of α′-martensite, the single-variant α′-martensite has a higher strain energy density than the multi-variant one. As the volume fraction of α′-martensite increases, the strain energy density difference between multi-variant and single-variant increases. Previous studies have demonstrated that increasing the strain energy density has a negative effect on the growth of α′-martensite [33,34]. The calculated strain energy density results clearly show that variant selection for dynamic strain tests can account for the limited α′-martensite growth.

Therefore, overall, there is a correlation between high strain rates and variant selection, which suppresses α′-martensite growth. Vázquez-Fernández et al. [10] suggested that high-strain-rate-based variant selection results in α′-martensite nucleation in a restricted habit plane. Other studies suggested that martensitic transformation sequences have a significant influence on the α′-martensite variant [25,35]. Wang et al.'s study [25,36] found significant differences in variant selection between γ→ε→α' and γ→α' sequences. In that study, the α′ phase nucleated from

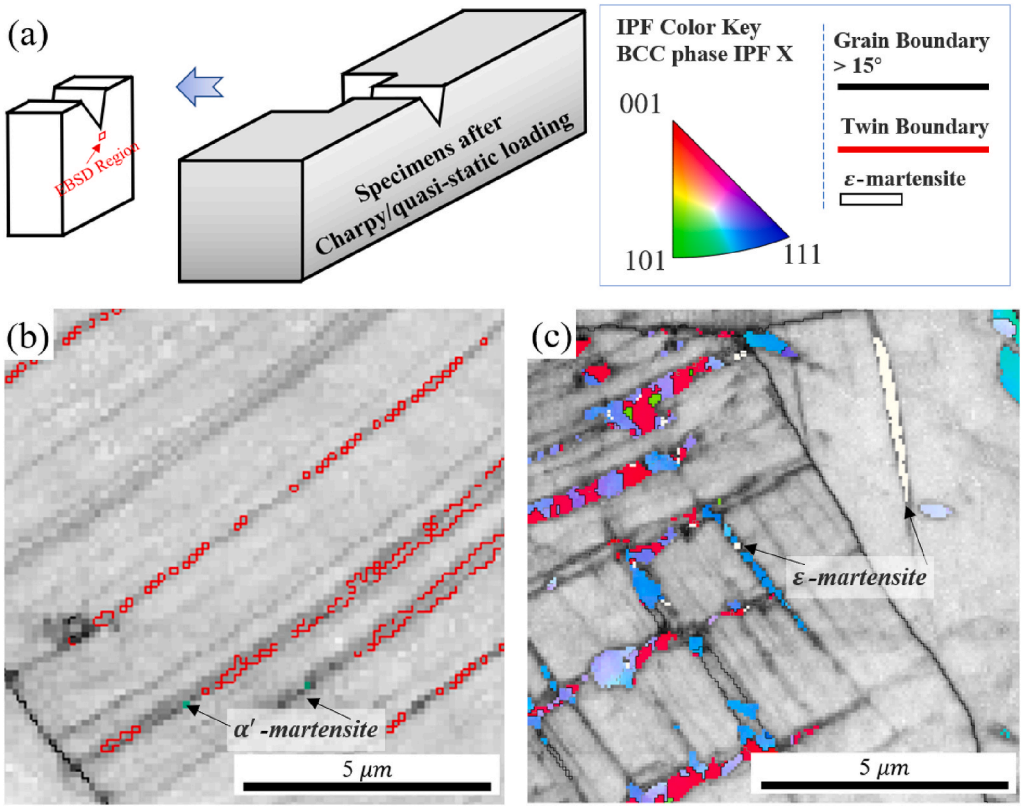

Fig. 8. (a) Schematic diagram of EBSD region; (b) Charpy specimen subjected to dynamic loading conditions with 2% nominal strain; (c) Charpy specimen subjected to quasi-static loading conditions with 2% nominal strain.

ε forms with multi-variant instead of single-variant α′-martensite. Additionally, when α′ is directly nucleated at austenite thin slip-bands, a single-variant forms. For the γ→ε→α′ sequence, the α′ variant with the highest transformation priority forms first, but with increasing deformation, the variant pair is formed, resulting in multi-variant α′-martensite. For the γ→α′ sequence, a single α′ variant nucleates at defective austenite, then continuously grows as the deformation increases. Thus, based on the α′-martensite growth sites, the variant selection caused by the high strain rate results in a higher elastic strain energy, which suppresses the growth of α′-martensite and reduces the final volume fraction of this variant.

3.4. A further study for validate the results of quasi-in-situ EBSD results

In-situ and quasi-in-situ EBSD technology has been widely used in the martensitic transformation field [37,38], due to its characterization directly and traceability. However, it also possesses some shortcomings, the most significant one is that the stress state of sample surface grains is quite different from the bulk body grains. I.e. the sample surface of the observed area in the in-situ test is under a free-standing condition. Thus,

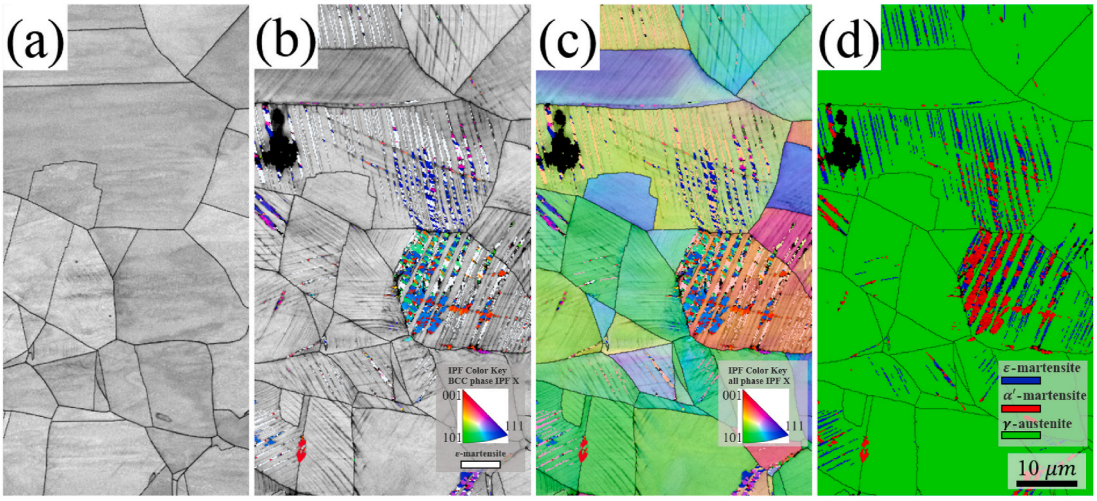

Fig. 9. Colored BCC IPF X, white ε-martensite phase, and BC map of a specific area subjected to dynamic-loading conditions at −25 °C with (a) 0% and (b) 2% nominal strain, (c) IPF X map of all phases, and (d) phase map (green for austenite phase, blue for ε-martensite phase, and red for α′-martensite phase). (For interpretation of the references to color in this figure legend, the reader is referred to the Web version of this article.)

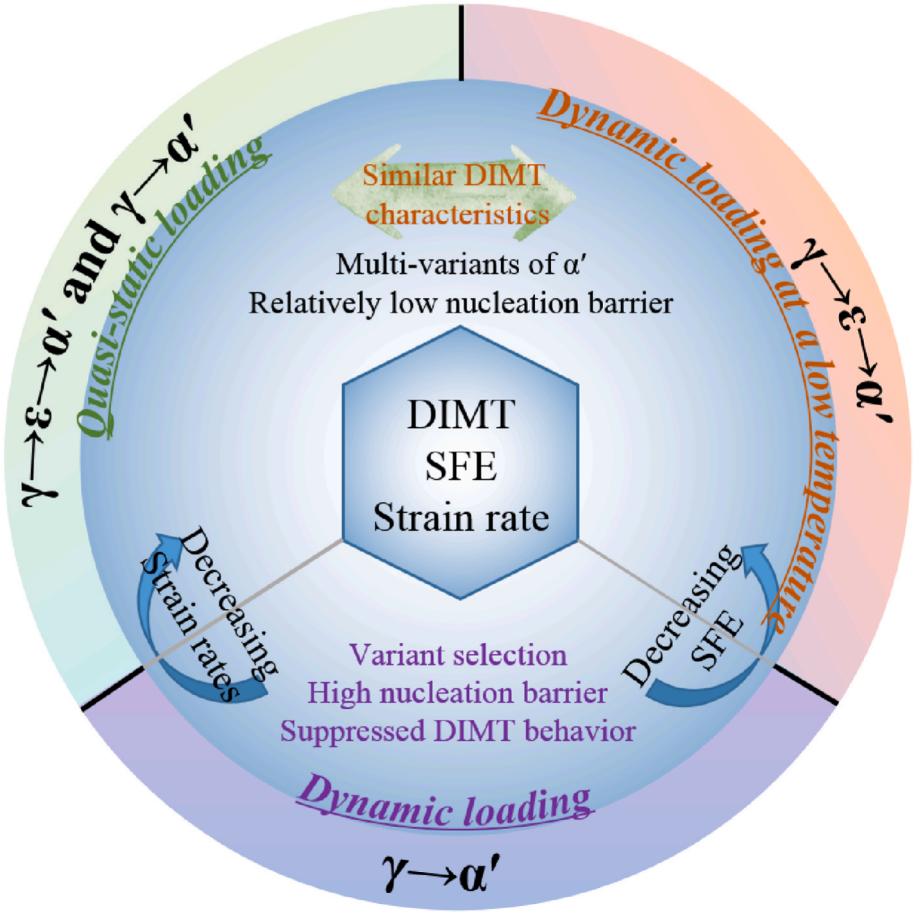

Fig. 10. Schematic diagram of DIMT behavior related to strain rates and SFE.

aims to prove and confirm the results in the in-situ study reliable and typically, a study about the deformation product at the bulk body grains has been carried out.

Standards Charpy samples were fabricated and then deformed under quasi-static loading and Charpy impact loading to 2% nominal strain respectively. The tested samples were divided along the mid of Charpy samples, as schematically illustrated in Fig. 8(a). Then EBSD test was carried out, as shown in Fig. 8 (b and c) represented for Charpy impact and quasi-in-situ loading respectively. In which, the red line represents for twin boundary, white represents for ε-martensite and colored represents forα'-martensite IPF X. It's clearly shown that deformation twins and ε-martensite plays a dominant role in Charpy impact and quasi-static loading respectively. Consistent with the quasi-in-situ EBSD results, that $\gamma\rightarrow\alpha'$ occurs in Charpy impact test while $\gamma\rightarrow\varepsilon\rightarrow\alpha'$ occurs in quasi-static loading condition.

4. Discussion

4.1. Relationship between high-strain-rate-induced variant selection and ambient temperature

As claimed in the previous sections, the high-strain-induced variant-selection phenomenon plays a significant role in suppressing the nucleation and growth of α'-martensite, which is unfavorable for DIMT. However, the existence of ε-martensite was proven to benefit the formation of multi-variants [25,36]. Thus, additional dynamic tests below -25 °C were performed to tailor the martensitic transformation sequences. Similarly, the quasi-in-situ EBSD results (Fig. 9) show that decreasing the temperature promoted the formation of ε-martensite under dynamic loading conditions, as expected. The variant pairs are presented in ε-martensite laths, as observed in our previous studies [25, 36], where the formation of variant pairs can be explained by their associated low transformation strain energy and interface energy [39]. The variant-selection phenomenon under dynamic-loading conditions is more likely to result in the $\gamma\rightarrow\alpha$' transformation route than the $\gamma\rightarrow\varepsilon\rightarrow\alpha$' one. Compared to the same strain conditions at 25 °C, a lower ambient temperature significantly facilitates DIMT. In the case that the $\gamma\rightarrow\varepsilon\rightarrow\alpha$' transformation route occurs on the crystallographic sites, the existence of ε-martensite could less suppressed DIMT behavior in the condition of high strain rate.

Based on the study of microstructural evolution at various conditions, similar martensitic transformation sequences were observed under quasi-static loading and dynamic loading at -25 °C, as summarized by the schematic in Fig. 10. The relatively high nucleation energy of α'-martensite and elastic strain energy density under dynamic loading are more likely to be related to the $\gamma\rightarrow\alpha$' martensitic transformation sequences.

4.2. Design strategies to facilitate TRIP effect based on control of martensitic transformation sequences

The suppressed DIMT behavior under dynamic loading conditions weakens the work-hardening properties, and thus, negatively influences the mechanical properties of TRIP-assisted steel. The volume fraction of DIMT largely depends on the martensitic transformation sequences, and the selection of the transformation sequences is generally a result of the SFE and Gibbs free energy. Thus, to facilitate TRIP behavior and optimize the work-hardening effect under high strain rates, accurate control of the SFE value is required. The following design strategies are therefore proposed. First, to reduce the initial SFE value of the steel, it is

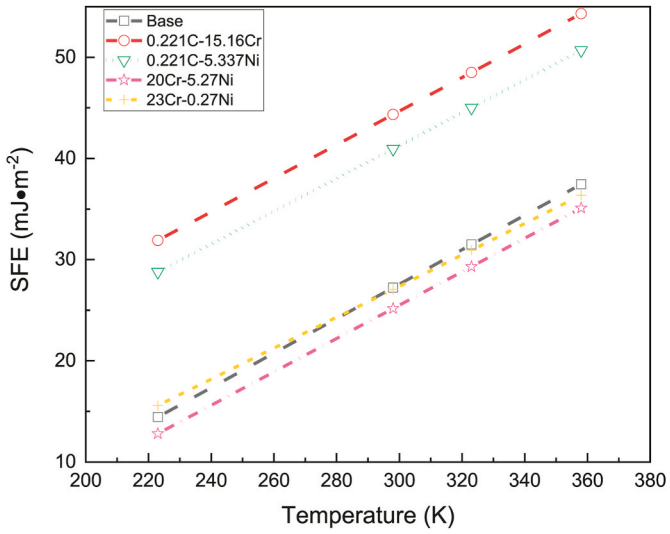

Fig. 11. SFE as a function of temperature for a range of austenitic steels.

important to ensure that the γ→ε→α' transformation occurs under high strain rates. This can be achieved by methods such as increasing the austenite grain size or reducing the fraction of the element (such as element Al, Ni, N, C, and etc). Second, to reduce the temperature sensitivity of the SFE, minimize the effect of the strain rate, and reduce the effect of adiabatic heating on the SFE; the Cr content can be increased based on the results of thermodynamics calculations (Fig. 11). In addition to precise control of the SFE, tailoring the Gibbs free energy should also be considered. Similar to a previous study of high-Mn steel [40], Mn-containing steel is more likely to form ε-martensite than Al-containing steel.

5. Conclusion

This study investigated the strain rate dependence of the α′-martensitic transformation in a metastable austenitic stainless steel. The α′-martensitic transformation sequences under dynamic (Charpy impact) and quasi-static loading tests were investigated by micro-beam XRD and quasi-in-situ EBSD. The role of the martensitic transformation sequence was identified as the key factor influencing DIMT behavior, which affects α′-martensitic nucleation and the elastic strain energy during the growth process. Based on the presented results, the following conclusions were drawn:

(1) At low strain rates, α′-martensite nucleates on both ε-martensite and twin/grain boundaries, and γ→ε→α′ and γ→α′ transformations occur. However, at higher strain rates, the nucleation favors the twin/grain boundaries, resulting in only γ→α′ transformation. The transition between these two strain-rate-dependent deformation mechanisms is attributed to the changes in SFE.
(2) The suppressed γ→ε→α′ transformation routes under dynamic loading conditions affects both nucleation and growth sites. First, it increases the nucleation barriers of α′-martensite, while during growth, variant selection occurred in the γ→α′ transformations sequences, resulting in unfavorably high elastic strain energy.
(3) To eliminate the adverse effects of adiabatic heating caused by high strain rates, two feasible strategies are proposed based on the tailoring of martensitic transformation routes: (i) reducing the initial SFE value; and (ii) decreasing the temperature sensitivity of the SFE.

Data availability statement

The raw data required to reproduce these findings are available upon reasonable request.

CRediT authorship contribution statement

Minghao Huang: Data curation, Writing – original draft. **Jiahua Yuan:** Data curation. **Jinliang Wang:** Formal analysis. **Lingyu Wang:** Writing – review & editing. **A. Mogucheva:** Supervision. **Wei Xu:** Funding acquisition, Supervision.

Declaration of competing interest

The authors declare that they have no known competing financial interests or personal relationships that could have appeared to influence the work reported in this paper.

Acknowledgements

The research was financially supported by the National Natural Science Foundation of China (No. U1808208and 51961130389) and National Key Research and Development Program (No. 2021YFE0204100) Major scientific and technological innovation projects of Shandong Province (Grant No. 2019TSLH0103).

References

[1] M. Soleimani, A. Kalhor, H. Mirzadeh, Transformation-induced plasticity (TRIP) in advanced steels: a review, Mater. Sci. Eng. 795 (2020) 140023, https://doi.org/10.1016/j.msea.2020.140023.
[2] M. Koyama, Z. Zhang, M.M. Wang, D. Ponge, D. Raabe, K. Tsuzaki, H. Noguchi, C. C. Tasan, Bone-like crack resistance in hierarchical metastable nanolaminate steels, Science 355 (2017) 1055–1057, https://doi.org/10.1126/science.aal2766.
[3] L. Samek, B.C.D. Cooman, J.V. Slycken, P. Verleysen, J. Degrieck, Physical metallurgy of multi-phase steel for improved passenger car crash-worthiness, Steel Res. 75 (2004) 716–723, https://doi.org/10.1002/srin.200405833.
[4] P.K. Xia, F.J.C. Rodríguez, I. Sabirov, Microstructure evolution and adiabatic heating during dynamic biaxial deformation of a 304 stainless steel, Mater. Sci. Eng., A 793 (2020) 139829, https://doi.org/10.1016/j.msea.2020.139829.
[5] Y.F. Shen, X.X. Li, X. Sun, Y.D. Wang, L. Zuo, Twinning and martensite in a 304 austenitic stainless steel, Mater. Sci. Eng., A 552 (2012) 514–522, https://doi.org/10.1016/j.msea.2012.05.080.
[6] X.C. Wei, R.Y. Fu, L. Li, Tensile deformation behavior of cold-rolled TRIP-aided steels over large range of strain rates, Mater. Sci. Eng., A 465 (2007) 260–266, https://doi.org/10.1016/j.msea.2007.02.126.
[7] H. Jin, B. Sanborn, W.Y. Lu, B. Song, Mechanical characterization of 304L-VAR stainless steel in tension with a full coverage of low, intermediate, and high strain rates, Mech. Mater. 152 (2021) 103654–103666, https://doi.org/10.1016/j.mechmat.2020.103654.
[8] K. Kishore, R.G. Kumar, A.K. Chandan, Critical assessment of the strain-rate dependent work hardening behaviour of AISI 304 stainless steel, Mater. Sci. Eng., A 803 (2021) 140675–140688, https://doi.org/10.1016/j.msea.2020.140675.
[9] J. Talonen, H. Hänninen, Formation of shear bands and strain-induced martensite during plastic deformation of metastable austenitic stainless steels, Acta Mater. 55 (2007) 6108–6118, https://doi.org/10.1016/j.actamat.2007.07.015.
[10] N.I. Vázquez-Fernández, T. Nyyssnen, M. Isakov, M. Hokka, V.T. Kuokkala, Uncoupling the effects of strain rate and adiabatic heating on strain induced martensitic phase transformations in a metastable austenitic steel, Acta Mater. 176 (2019) 134–144, https://doi.org/10.1016/j.actamat.2019.06.053.
[11] W.J. Dan, W.G. Zhang, S.H. Li, X.W. Song, Prediction of mechanical properties of TRIP590 steel with strain rate effect, Mater. Res. Innovat. 15 (2011) 90–93, https://doi.org/10.1179/143307511X12858956847273.
[12] S.H. Li, W.J. Dan, W.G. Zhang, Z.Q. Lin, A model for strain-induced martensitic transformation of TRIP steel with pre-strain, Comput. Mater. Sci. 40 (2007) 292–299, https://doi.org/10.1016/j.commatsci.2006.12.011.
[13] T. Masumura, N. Nakada, T. Tsuchiyama, S. Takaki, T. Koyano, K. Adachi, The difference in thermal and mechanical stabilities of austenite between carbon- and nitrogen-added metastable austenitic stainless steels, Acta Mater. 84 (2015) 330–338, https://doi.org/10.1016/j.actamat.2014.10.041.
[14] W.N. Zhang, Z.Y. Liu, Z.B. Zhang, G.D. Wang, The crystallographic mechanism for deformation induced martensitic transformation observed by high resolution transmission electron microscope, Mater. Lett. 91 (2013) 158–160, https://doi.org/10.1016/j.matlet.2012.09.086.
[15] W.J. Dan, W.G. Zhang, S.H. Li, Z.Q. Lin, A model for strain-induced martensitic transformation of TRIP steel with strain rate, Comput. Mater. Sci. 40 (2007) 101–107, https://doi.org/10.1016/j.commatsci.2006.11.006.

[16] O.M. Cohen, A General Mechanism of Martensitic Nucleation: Part II. FCC → BCC and Other Martensitic Transformations, Metallurgical & Materials Transactions A, 1976, https://doi.org/10.1007/BF02659823.
[17] K.P. Staudhammer, L.E. Murr, S.S. Hecker, Nucleation and evolution of strain-induced martensitic (b.c.c.) embryos and substructure in stainless steel: a transmission electron microscope study, Acta Metall. 31 (2) (1983) 267–274, https://doi.org/10.1016/0001-6160(83)90103-7.
[18] S. Lee, Y. Estrin, B.C.D. Cooman, Effect of the strain rate on the TRIP–TWIP transition in austenitic Fe-12 pct Mn-0.6 pct C TWIP steel, Metall. Mater. Trans. 45 (2014) 717–730, https://doi.org/10.1007/s11661-013-2028-9.
[19] P.J. Ferreira, J.B.V. Sande, M.A. Fortes, A. Kyrolainen, Microstructure development during high-velocity deformation, Metall. Mater. Trans. 35 (10) (2004) 3091–3101, https://doi.org/10.1007/s11661-004-0054-3.
[20] M.J. Sohrabi, M. Naghizadeh, H. Mirzadeh, Deformation-induced martensite in austenitic stainless steels: a review, Archives of Civil and Mechanical Engineering 20 (2020) 124, https://doi.org/10.1007/s43452-020-00130-1.
[21] J.T. Benzing, W.A. Poling, D.T. Pierce, J. Bentley, K.O. Findley, D. Raabe, J. E. Wittig, Effects of strain rate on mechanical properties and deformation behavior of an austenitic Fe-25Mn-3Al-3Si TWIP-TRIP steel, Mater. Sci. Eng., A 711 (2018) 78–92, https://doi.org/10.1016/j.msea.2017.11.017.
[22] S. Curtze, V.T. Kuokkala, Dependence of tensile deformation behavior of TWIP steels on stacking fault energy, temperature and strain rate, Acta Mater. 58 (15) (2010) 5129–5141, https://doi.org/10.1016/j.actamat.2010.05.049.
[23] R. Zaera, J.A. Rodríguez-Martínez, D. Rittel, On the Taylor–Quinney coefficient in dynamically phase transforming materials. Application to 304 stainless steel, Int. J. Plast. 40 (2013) 185–201, https://doi.org/10.1016/j.ijplas.2012.08.003.
[24] J.T. Benzing, Y. Liu, X. Zhang, W.E. Luecke, J.E. Wittig, Experimental and numerical study of mechanical properties of multi-phase medium-Mn TWIP-TRIP steel: influences of strain rate and phase constituents, Acta Mater. 177 (2019) 250–265, https://doi.org/10.1016/j.actamat.2019.07.036.
[25] J.L. Wang, M.H. Huang, J. Hu, C.C. Wang, W. Xu, EBSD investigation of the crystallographic features of deformation-induced martensite in stainless steel, J. Mater. Sci. Technol. 69 (2021) 148–155, https://doi.org/10.1016/j.jmst.2020.08.023.
[26] P. Barriobero-Vila, R. Jerez-Mesa, A. Guitar, O. Gavalda-Diaz, J.A. Travieso-Rodríguez, A. Stark, N. Schell, J. Llumà, G. Fargas, A. Mateo, J.J. Roa, Deformation kinetics of a TRIP steel determined by in situ high-energy synchrotron X-ray diffraction, Materialia (2021) 101251.
[27] B.G. Olson, M. Cohen, A mechanism for the strain-induced nucleation of martensitic transformations, J. Less Common Met. 28 (1972) 107–118, https://doi.org/10.1016/0022-5088(72)90173-7.
[28] E. Polatidis, W.N. Hsu, M. Smíd, T. Panzner, S. Chakrabarty, P. Pant, H. V. Swygenhoven, Suppressed martensitic transformation under biaxial loading in low stacking fault energy metastable austenitic steels, Scripta Mater. 147 (2018) 27–32, https://doi.org/10.1016/j.scriptamat.2017.12.026.
[29] S. Curtze, V.T. Kuokkala, A. Oikari, J. Talonen, H. Hanninen, Thermodynamic modeling of the stacking fault energy of austenitic steels, Acta Mater. 59 (2011) 1068–1076, https://doi.org/10.1016/j.actamat.2010.10.037.
[30] Y. Tomota, M. Strum, J.W. Morris, The relationship between toughness and microstructure in Fe-high Mn binary alloys, Metall. Mater. Trans. 18 (13) (1987) 1073–1081, https://doi.org/10.1007/BF02668556.
[31] S. Morito, H. Tanaka, R. Konishi, T. Furuhara, T. Maki, The morphology and crystallography of lath martensite in Fe-C alloys, Acta Mater. 51 (6) (2003) 1789–1799, https://doi.org/10.1016/S1359-6454(02)00577-3.
[32] H.K. Yeddu, A. Borgenstam, J. Ågren, Stress-assisted martensitic transformations in steels: a 3-D phase-field study, Acta Mater. 61 (7) (2013) 2595–2606, https://doi.org/10.1016/j.actamat.2013.01.039.
[33] A. Artemev, Y. Jin, A.G. Khachaturyan, Three-dimensional phase field model of proper martensitic transformation, Acta Mater. 49 (7) (2001) 1165–1177, https://doi.org/10.1016/S1359-6454(01)00021-0.
[34] H.K. Yeddu, V.I. Razumovskiy, A. Borgenstam, P.A. Korzhavyi, A.V. Ruban, J. Ågren, Multi-length scale modeling of martensitic transformations in stainless steel, Acta Mater. 60 (2012) 6508–6517, https://doi.org/10.1016/j.actamat.2012.08.012.
[35] M. Humbert, B. Petit, B. Bolle, N. Gey, Analysis of the γ–ε–α′ variant selection induced by 10% plastic deformation in 304 stainless steel at -60°C, Mater. Sci. Eng., A 454 (2007) 508–517, https://doi.org/10.1108/00220410810884101.
[36] J.L. Wang, M.H. Huang, X.H. Xi, C.C. Wang, W. Xu, Characteristics of nucleation and transformation sequence in deformation-induced martensitic transformation, Mater. Char. 163 (2020) 110234, https://doi.org/10.1016/j.matchar.2020.110234.
[37] M.M. Wang, Z.M. Li, D. Raabe, In-situ SEM observation of phase transformation and twinning mechanisms in an interstitial high-entropy alloy, Acta Mater. 147 (2018) 236–246, https://doi.org/10.1016/j.actamat.2018.01.036.
[38] M.M. Wang, C.C. Tasan, D. Ponge, A. Kostka, D. Raabe, Smaller is less stable: size effects on twinning vs. transformation of reverted austenite in TRIP-maraging steels, Acta Mater. 79 (2014) 268–281, https://doi.org/10.1016/j.actamat.2014.07.020.
[39] Y. Higo, F. Lecroisey, T. Mori, Relation between applied stress and orientation relationship of α′ martensite in stainless steel single crystals, Acta Metall. 22 (1974) 313–323, https://doi.org/10.1016/0001-6160(74)90170-9.
[40] S.S. Sohn, S. Hong, J. Lee, B.C. Suh, S.K. Kim, B.J. Lee, N.J. Kim, S. Lee, Effects of Mn and Al contents on cryogenic-temperature tensile and Charpy impact properties in four austenitic high-Mn steels, Acta Mater. 100 (2015) 39–52, https://doi.org/10.1016/j.actamat.2015.08.027.